

1 **Turbulence characteristics and mixing properties of gravity currents over complex**
2 **topography**

3 Maria Rita Maggi,^{1, a)} M. Eletta Negretti,² Emil Hopfinger,² and Claudia Adduce¹

4 ¹⁾*Department of Engineering, Roma Tre University, Via Vito Volterra 62, 00146,*
5 *Rome, Italy*

6 ²⁾*Univ. Grenoble Alpes, CNRS, Grenoble INP, LEGI, 38000, Grenoble,*
7 *France*

8 (Dated: 2 November 2022)

9 Understanding gravity currents developing on complex topography, that involve tur-
10 bulence and mixing processes on a wide range of spatial and temporal scales, is of
11 importance for estimating near ground fluxes in oceanic and atmospheric circulation.
12 We present experimental results, based on high resolution velocity and density mea-
13 surements, of constant upstream buoyancy supply gravity currents flowing from a
14 horizontal boundary onto a tangent hyperbolic shaped slope. The mean flow, the
15 turbulence characteristics and mixing properties, the latter expressed in terms of
16 mixing lengths and eddy coefficients, are determined, highlighting their dependency
17 on topography. These mean flow and mixing characteristics are compared with the
18 field measurements in katabatic winds by Charrondière, Hopfinger, and Brun¹ ; **the**
19 **latter are gravity flows that develop over sloping terrain due to radiative cooling at**
20 **the surface. The results obtained show** that the mean katabatic flow structure is
21 substantially different from that of the upstream buoyancy supply gravity current.
22 However interestingly, dimensionless mixing lengths and eddy coefficients compare
23 well despite the difference in mean flow structure and a two order of magnitude
24 difference in the Reynolds number.

^{a)}Electronic mail: mariarita.maggi@uniroma3.it

I. INTRODUCTION

Gravity currents are frequent in the natural environment with the density difference being due to temperature, salinity, dissolved substances, or particles within the flow. Examples of such currents in the atmosphere and oceans are sea breeze fronts², katabatic winds³⁻⁶, continental slope boundary currents⁷, turbidity currents⁸ including avalanches⁹ and exchange flows¹⁰⁻¹⁴. For these reasons investigations of gravity currents in the context of their many applications have been numerous and of interdisciplinary nature. Several studies have shown how the propagation of dense, bottom gravity currents is affected by topographic aspects¹⁵⁻²², by sloping boundaries²³⁻³⁰ as well as rapidly changing slopes³¹⁻³⁴. Most of these studies have focused on the mean flow dynamics and the related entrainment of ambient fluid that strongly affects the flow development and fluid properties. Entrainment is related with the type of interfacial instability³⁵⁻³⁷ that also depends on initial conditions and slope angle^{32,33}.

Gravity currents involve a large variety of different processes, e.g. flow instabilities, boundary layers, vortices and internal waves, which occur in very localized regions, so that they cannot be resolved in oceanic and atmospheric circulation models³⁸. Since these currents affect the general circulation³⁹, a parametrization of their effect is necessary, which requires the determination of the involved turbulent and mixing processes.

Modern experimental techniques allow high quality, quantitative measurements of the mean flow development and entrainment, the turbulence characteristics, and internal mixing. Measurements of eddy coefficients and mixing lengths have been conducted in the outer part of a gravity current by Odier *et al.*⁴⁰ and in lock exchange gravity currents by Balasubramanian and Zhong⁴¹, Agrawal *et al.*⁴², Mukherjee and Balasubramanian^{43,44}. Measurements in katabatic winds on glaciers and alpine slopes have been performed by Princevac, Hunt, and Fernando⁴, Monti, Fernando, and Princevac⁴⁵, Charrondière *et al.*⁴⁶, who focused on mean flow oscillations and turbulence characteristics and, more recently, on mixing length and eddy coefficients⁶.

Here, we present results from laboratory experiments of continuously supplied saline gravity currents flowing onto a complex topography of tangent hyperbolic shape that reproduces a typical alpine topography⁵. Emphasis is placed on the turbulence and mixing characteristics in the different regions of the gravity current down the slope. Comparison of the present results with those obtained in the laboratory by Odier, Chen, and Ecke⁴⁷

56 and by Charrondière *et al.*⁶ in katabatic winds is performed. The latter is of particular
 57 interest because Reynolds numbers and scales are widely different. Furthermore, most of
 58 the experimental data of katabatic winds have been obtained in a limited region above the
 59 maximum-wind-speed height where mixing lengths increase with height. Thus, laboratory
 60 results can shed new light on katabatic wind mixing behaviour.

61 The paper is organized as follows: the essential details of the experimental apparatus
 62 and measurements techniques are given in Sec.II, including a general description of the
 63 flow development. Results of the mean flow development, mixing properties and Reynolds
 64 stresses are discussed in Sec.III. A comparison of some mean flow, mixing length and
 65 eddy coefficients of the present experiments with previous studies⁴⁷ and especially with the
 66 katabatic wind results of Charrondière, Hopfinger, and Brun¹ is presented in Sec.IV. Sec.V
 67 summarizes the results and includes concluding remarks.

68 II. EXPERIMENTAL DESIGN

69 The experiment, sketched in figure 1a and described in detail elsewhere^{32,33}, consists of
 70 a saline gravity current initiated by injecting a constant flow rate Q_0 upstream of a 25cm
 71 wide and 160cm long horizontal channel within a lighter ambient fluid (ethanol solution
 72 for refractive index matching). The horizontal channel is followed by a hyperbolic tangent
 73 profiled slope boundary (cf. figure 1b), defined as:

$$74 \quad y = \frac{h_c}{2}(1 - \tanh(x)), \quad \theta = \operatorname{atan}\left(-\frac{h_c}{2}(1 - \tanh(x^2))\right) \quad (1)$$

75 No return flow and a constant total water depth of $h = 20 \pm 0.5$ cm in the initial horizontal
 76 channel were assured by evacuating the same volume as supplied at the downstream end of
 77 the experimental channel.

78 Fig.2 presents one series of snapshots of one experiment with dye added in the saline
 79 water ($D5_2$, cf. table I) after the current has reached stationary conditions (i.e. after the
 80 initial passage of the gravity current head). Two different types of shear instabilities at
 81 the interface between the dense flow and the ambient fluid can be recognized: Holmboe
 82 instability (HI)⁴⁸ near slope begin, followed by Kelvin–Helmholtz instabilities (KHI) on
 83 the steepest part of the slope. The final portion and the downstream part of the slope are
 84 characterized by the collapse of the KHIs which generate a turbulent (mixed) shear layer

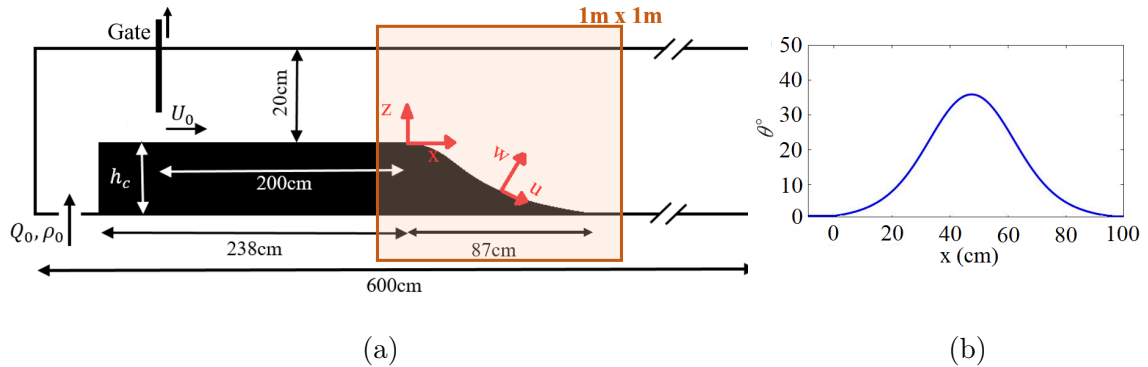


FIG. 1. a) Schematic side-view of the tank used to perform laboratory experiments with the main geometrical features and the notations. b) Slope angle evolution along the x (down slope) direction.

86 (TSL) with an intermediate upper density layer.

87 A total of 12 experiments have been performed by varying the initial density difference
 88 $\Delta\rho$ between the current and the ambient water and Q_0 (see table I). The optical non-
 89 intrusive experimental technique PIV was adopted to measure the instantaneous velocity
 90 field in 9 experiments, while the fluorescent dye was added to the saline injected solution
 91 to determine the local relative density difference in further 3 experiments for evaluating the
 92 gradient Richardson number (cf. table I).

93 For the PIV measurements, a CCD camera (1200x1600 pixels) was used to acquire the
 94 experimental images with an acquisition frequency of 23.23Hz. The camera allowed to
 95 record the whole slope field with an image size of 1m \times 1m. Each vector of the resulting field
 96 represents an area of approximately 0.23cm \times 0.23cm. Further details on the PIV procedure
 97 are given in Martin, Negretti, and Hopfinger³³.

98 To estimate relative averaged density profiles, a local calibration procedure taking into
 99 account the light absorption of Rhodamine 6G added to the injected saline water has been
 100 adopted. Details of the procedure can be found in Negretti, Zhu, and Jirka⁴⁹.

101 III. EXPERIMENTAL RESULTS

102 A. Mean flow development and entrainment

103 The along-slope mean velocity u and slope normal velocity w have been measured at
 104 three downstream positions x and are processed in experiments $R5_2$, $R15_2$ and $R15_3$ that

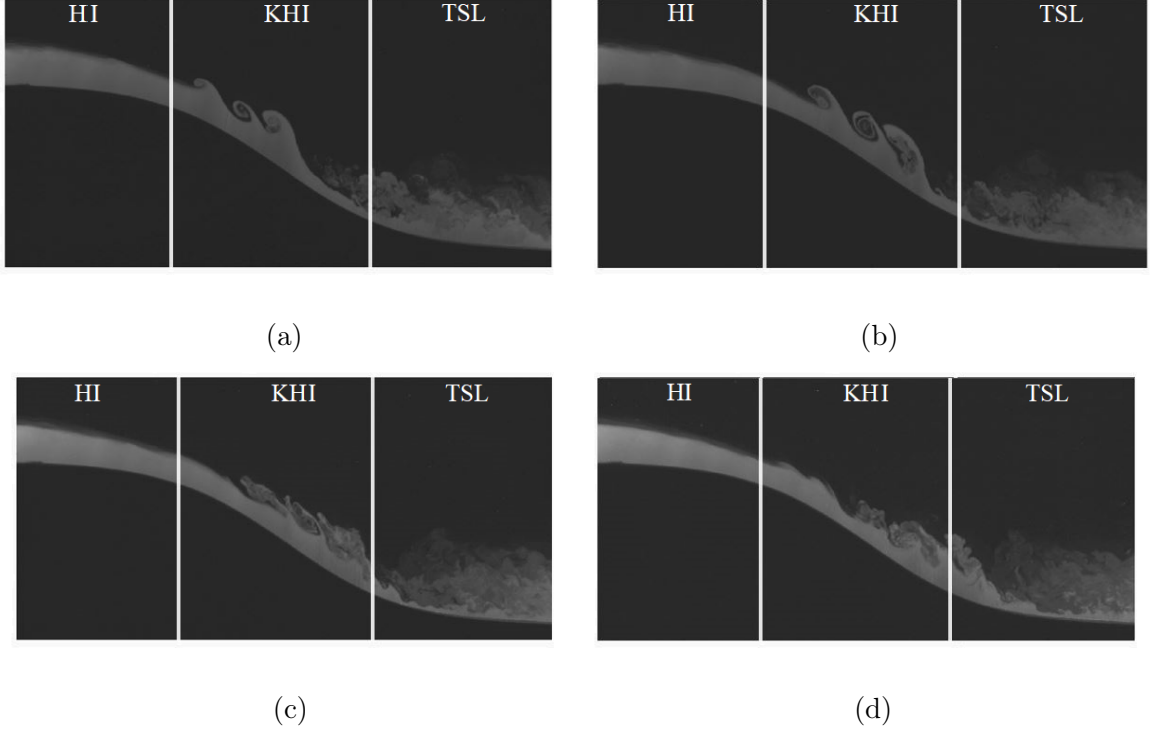


FIG. 2. Instantaneous images of dye visualizations of a gravity current with $q_0 = 45.76\text{cm}^2\text{s}^{-1}$ and $g'_0 = 5\text{cm s}^{-2}$. (a) $t = t_0$; (b) $t = t_0 + 0.01\text{s}$; (c) $t_0 + 0.02\text{s}$ and (d) $t_0 + 0.03\text{s}$. Three different zones can be defined that are characterized by different interface instabilities: Holmboe instability (HI) near slope begin, Kelvin–Helmholtz instability (KHI) at steep slope and the final area of KHI collapse to a turbulent (mixed) shear layer (TSL).

105 are representative of all the experiments conducted. These show how a change in g'_0 and q_0
 106 affect the flow. As in Negretti, Flør, and Hopfinger³² and Martin, Negretti, and Hopfinger³³,
 107 the flow distance x has been normalized by h_{0i} , the initial mean height of the dense current
 108 at slope begin, i.e. $x^* = x/h_{0i}$.

109 Fig.3 shows time-averaged along-slope velocity $\langle u \rangle$ and slope normal velocity $\langle w \rangle$ at three
 110 positions $x^* = 1$, $x^* = 7$ and $x^* = 11$ indicated by the continuous vertical black lines in
 111 Fig.3a. Upstream of the slope, the current has a constant $\langle u \rangle$ as long as the change in the
 112 bottom inclination does not affect the flow. Then, $\langle u \rangle$ increases until KHI develop, which
 113 cause the slow down of the current followed by a nearby maximum constant velocity, which
 114 is reached from $x^* \approx 7$ as seen the in the insets in Fig.4.

115 Fig.3b-d show the $\langle u \rangle$ velocity profile and Fig.3c-g the slope normal velocity distribution
 116 $\langle w \rangle$ at $x^* = 1$ (a,d), $x^* = 7$ (b,e) and $x^* = 11$ (c,f). The different symbol colors indicate

TABLE I. Parameters of the experiments conducted, where q_0 is the dense flow rate per unit width, g'_0 the reduced gravity, $Re_0 = q_0/\nu$ is the inlet Reynolds number, $B_0 = q_0g'_0$ is the initial buoyancy flux and h_{0i} is the initial height of the dense current in the horizontal part of the channel.

Run	$q_0(\text{cm}^2\text{s}^{-1})$	$g'_0(\text{cm s}^{-2})$	Re_0	$B_0(\text{cm}^3\text{s}^{-3})$	$h_{0i}(\text{cm})$
$R5_1$	32.28	5	3200	160	6
$R5_2$	45.76	5	4600	225	6.7
$R5_3$	57.24	5	5700	280	7.5
$R10_1$	32.28	10	3200	320	5.8
$R10_2$	45.76	10	4600	460	6.3
$R10_3$	57.24	10	5700	570	7
$R15_1$	32.28	15	3200	485	5.7
$R15_2$	45.76	15	4600	685	6
$R15_3$	57.24	15	5700	860	6.4
$D5_1$	32.28	5	3200	160	6
$D5_2$	45.76	5	4600	225	6.7
$D5_3$	57.24	5	5700	280	7.5

117 different experiments, while the symbol shape refers to the position x^* .

118 In Fig.3a-c all the experiments show velocity profiles $\langle u \rangle$ similar to that of a plane turbu-
119 lent wall jet⁵⁰ as has also been observed by Buckee, Kneller, and Peakall⁵¹ and Ottolenghi
120 *et al.*⁵². The height where maximum velocity occurs is conditioned by interfacial drag. The
121 maximum velocity moves closer to the bottom as x^* increases. Fig.3d-f shows the time-
122 average vertical velocity $\langle w \rangle$. At $x^* = 1$ $\langle w \rangle$ is negative from the slope bottom up to the
123 shear layer where it tends to zero. The behaviour is opposite at $x^* = 7$, where the slope is
124 steepest with $\langle w \rangle$ being negative in the outer part of the current and in the ambient fluid.
125 Further downstream at $x^* = 11$ $\langle w \rangle$ weakly decreases with increasing z .

126 In order to highlight more clearly the change in flow structure with downstream distance
127 it is of interest to present velocities in dimensionless form. Fig.4 shows the variation along
128 $z/z_{0.5}$ of the dimensionless longitudinal velocity $\langle u \rangle / \langle u_m \rangle$ (symbols outlined in blue) and of
129 the normal component $\langle w \rangle / \langle u_m \rangle$ (symbols outlined in black) for experiments $R5_2$ (a) and
130 $R15_3$ (b), where $\langle u_m \rangle$ is the maximum mean velocity, shown in the insets, and $z_{0.5}$, is the

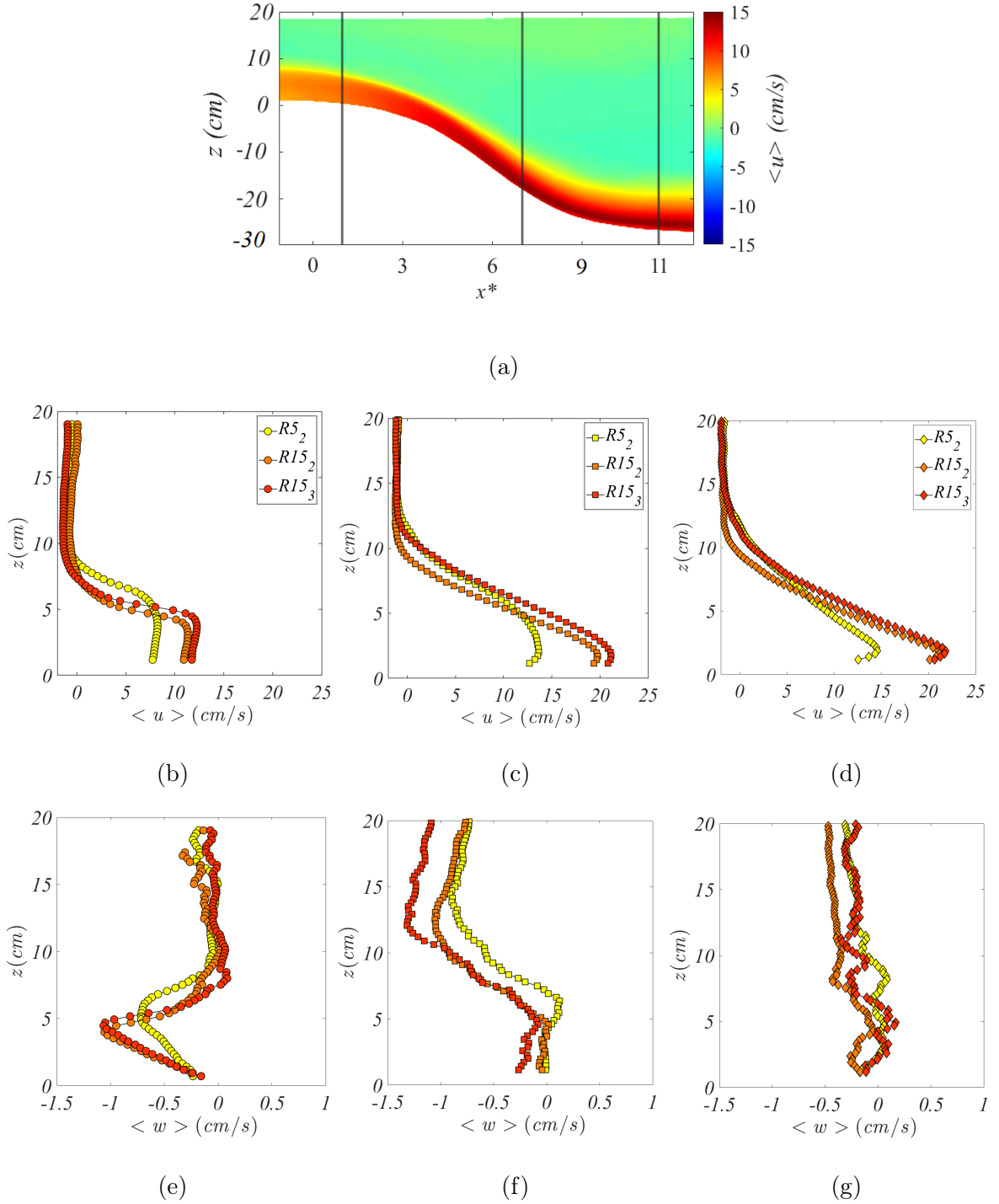


FIG. 3. Time-averaged along-slope velocity $\langle u \rangle$ and slope normal velocity $\langle w \rangle$ at positions $x^* = 1, 7, 11$ for experiments $R5_2$, (b–e), $R15_2$, (c–f) and $R15_3$, (d–g); (a), color plot of velocity $\langle u \rangle$ vs x^* for $R15_2$ with the vertical continuous lines indicating the positions $x^* = 1$, $x^* = 7$ and $x^* = 11$ where the time-averaged streamwise velocity profiles and the vertical velocity have been measured.

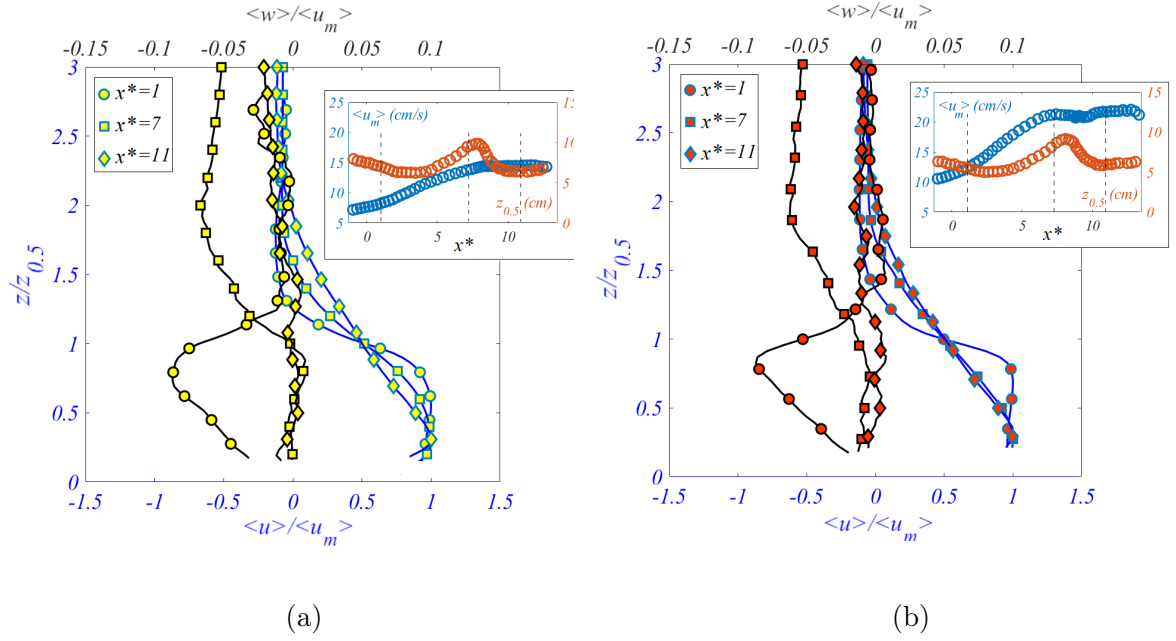


FIG. 4. Dimensionless profiles of the averaged streamwise velocity $\langle u \rangle / \langle u_m \rangle$ and vertical velocity $\langle w \rangle / \langle u_m \rangle$ for the experiments $R5_2$ (a) and $R15_3$ (b). The insets show time-average maximum values of the streamwise velocity component $\langle u_m \rangle$ in blue and the $z_{0.5}$ in red with the vertical continuous lines indicating the positions $x^* = 1, 7$ and 11 .

131 distance from the boundary where the velocity $\langle u \rangle$ is $\langle u_m \rangle / 2$. The maximum mean velocity,
 132 $\langle u_m \rangle$, and $z_{0.5}$ are shown in blue and orange respectively in the insets at the top right in
 133 Fig.4(a) and (b). Both experiments show a similar trend of $z_{0.5}$ and $\langle u_m \rangle$. In accordance
 134 with what was mentioned already above, it can be seen (compare insets) that higher g'_0 and
 135 q_0 lead to a higher $\langle u_m \rangle$, which increases along x^* until it reaches an almost constant value
 136 at $x^* > 7$. The change in $z_{0.5}$ is more complex. Upstream of the slope, $z_{0.5}$ is nearly constant
 137 while at slope begin first decreases and then increases smoothly in the deepest part of the
 138 slope due to the formation of KHI. Toward the end of the slope there is a rapid decrease
 139 of $z_{0.5}$ toward a constant value. As expected, the dimensionless velocity distributions and
 140 values are practically the same in experiments $R5_2$ and $R15_3$.

142 Calculating entrainment is of interest because it expresses mixing with the ambient fluid,
 143 related with interfacial instability, and interfacial drag. Following Morton, Taylor, and
 144 Turner⁵³, entrainment of ambient fluid is related with the normal velocity w_h at the interface

145 with the entrainment coefficient defined by:

$$146 \quad E_w = -\frac{w_h}{U}, \quad (2)$$

147 where U is the depth integrated velocity of the current. A cross-stream location $z/z_{0.5} \approx 1.5$
 148 has been chosen as the interface. Then, the velocity w_h at this location has been obtained
 149 from the PIV velocity data (Fig 3 and 4) by taking the average of three values of the normal
 150 velocity around $z/z_{0.5} = 1.5$. Invariance of the results has been checked by comparison be-
 151 tween results obtained directly from averaged velocity fields and from instantaneous velocity
 152 fields. We note that, as already reported by Odier, Chen, and Ecke³⁶ and Martin, Negretti,
 153 and Hopfinger³³ this definition of entrainment coefficients gives values somewhat larger than
 154 those obtained with the definition using the volume flux change in the downstream direction,
 155 $E_q = 1/Ud(Uh)/dx$ (cf. also Fig. 6).

156 Fig.5a shows the time-averaged entrainment coefficients E_w versus x^* for $R5_2$, $R15_2$ and
 157 $R15_3$ experiments. Despite the different initial conditions, E_w shows a similar behavior in
 158 all experiments. The entrainment rates are almost zero during the initial acceleration phase
 159 ($0 < x^* < 2$) and increase rapidly as KHI develop to reach maximum values at the steepest
 160 part of the slope ($x^* \approx 7$) and then decreases again in the TSL region. To highlight the
 161 effect of slope variation on entrainment, Fig.5(b-d) report the entrainment E_w evaluated at
 162 $x^* = 1$ (b), $x^* = 7$ (c) and $c^* = 11$ (d) as a function of the injected buoyancy flux B_0 for all
 163 the performed experiments.

164 In Fig.6 the entrainment coefficient E_w and E_q are plotted as a function of the local
 165 Froude number $Fr = Ri_g^{-0.5}$ and compared with other experimental data. The present data
 166 are for the range $0.5 < x^* < 1.5$, $6.5 < x^* < 7.5$ and $10.5 < x^* < 11.5$ and for experiments in
 167 which both velocity and density field measurements are available. To compute the Froude
 168 number, the gradient Richardson number $Ri_g = N^2 \cos \theta / S^2$ ($Fr = 1/\sqrt{Ri_g}$) has been used,
 169 where $N = \sqrt{-g\langle \delta_z \rho \rangle / \langle \rho \rangle}$ and $S = \langle \delta_z u \rangle$ represent the Brunt-Väisälä frequency and the
 170 vertical shear of velocity, respectively. We see that the data of the present study are in good
 171 agreement with those of previous studies.

172 B. Reynolds stresses

173 Key quantities for describing turbulence processes are the Reynolds stresses expressing
 174 turbulent transport of momentum⁵⁹. Fig.7 displays the variation with $z/z_{0.5}$ of the time

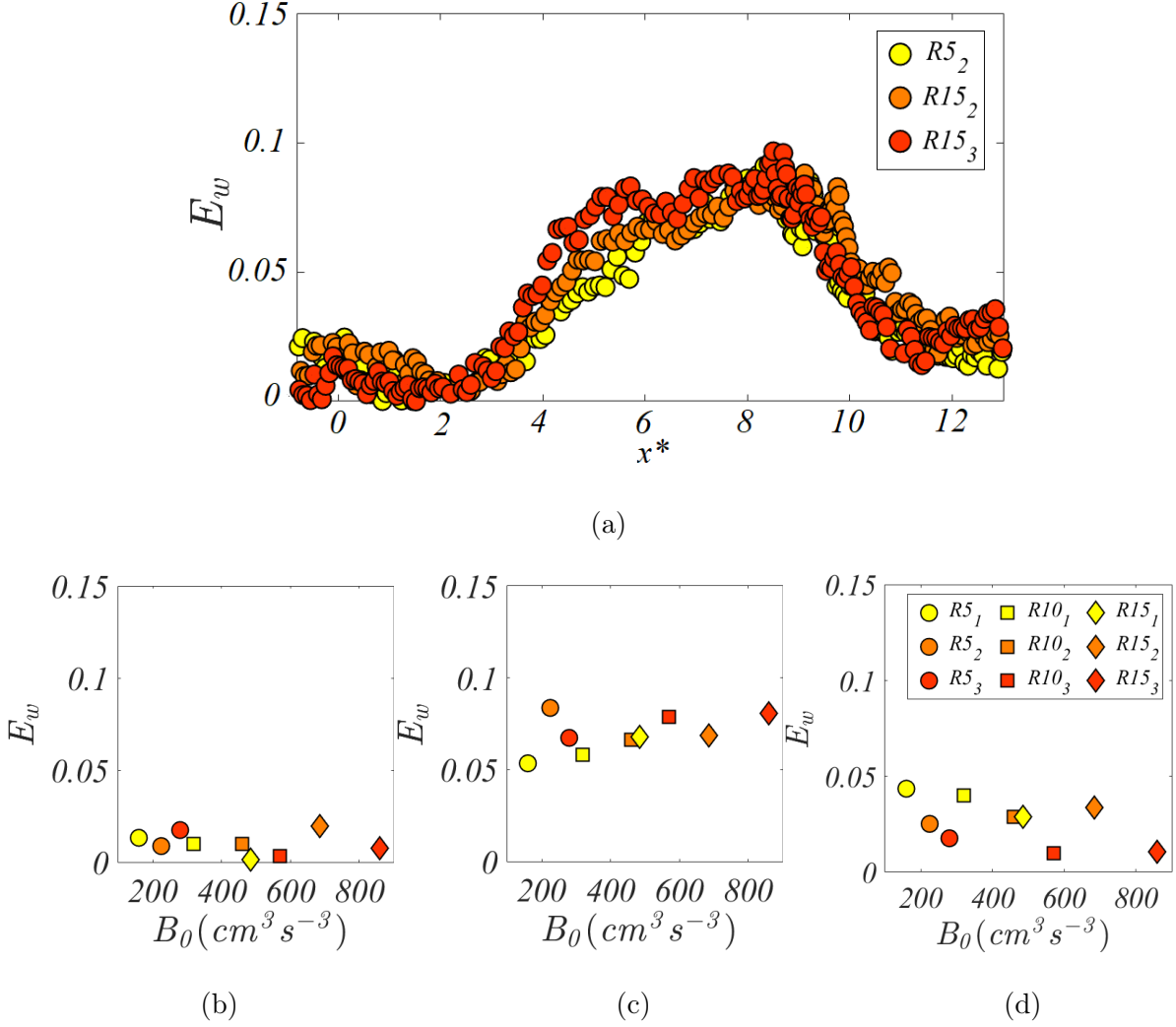


FIG. 5. a) Time-averaged entrainment coefficients E_w versus x^* for experiments $R5_2$, $R15_2$ and $R15_3$. Entrainment coefficient E_w versus initial buoyancy flux B_0 , at $x^* = 1$ (b), $x^* = 7$ (c) and $x^* = 11$ (d) for all performed experiments.

175 averaged Reynolds stresses $\langle u'u' \rangle / \langle u_m^2 \rangle$, (a,b) and of $\langle w'w' \rangle / \langle u_m^2 \rangle$ (c,d) at $x^* = 7$ and $x^* = 11$
 176 for experiments $R5_2$, $R15_2$ and $R15_3$. As expected, low values are observed close to the
 177 velocity maximum, increasing toward the wall (in the boundary layer, not shown here) and
 178 values are maximum in the outer shear layer^{60,61}.

179 The maximum values of the normal Reynolds stresses $\langle u'u' \rangle / \langle u_m^2 \rangle$ and $\langle w'w' \rangle / \langle u_m^2 \rangle$ at
 180 $x^* = 7$ have a near Gaussian distribution and are located close to $z/z_{0.5} = 1$ (see Fig.7a,c).
 181 In the experiments with larger density difference ($R15_{2,3}$), the values are lower and more
 182 spread out. The explanation for this behaviour is the difference in the mean velocity profiles.

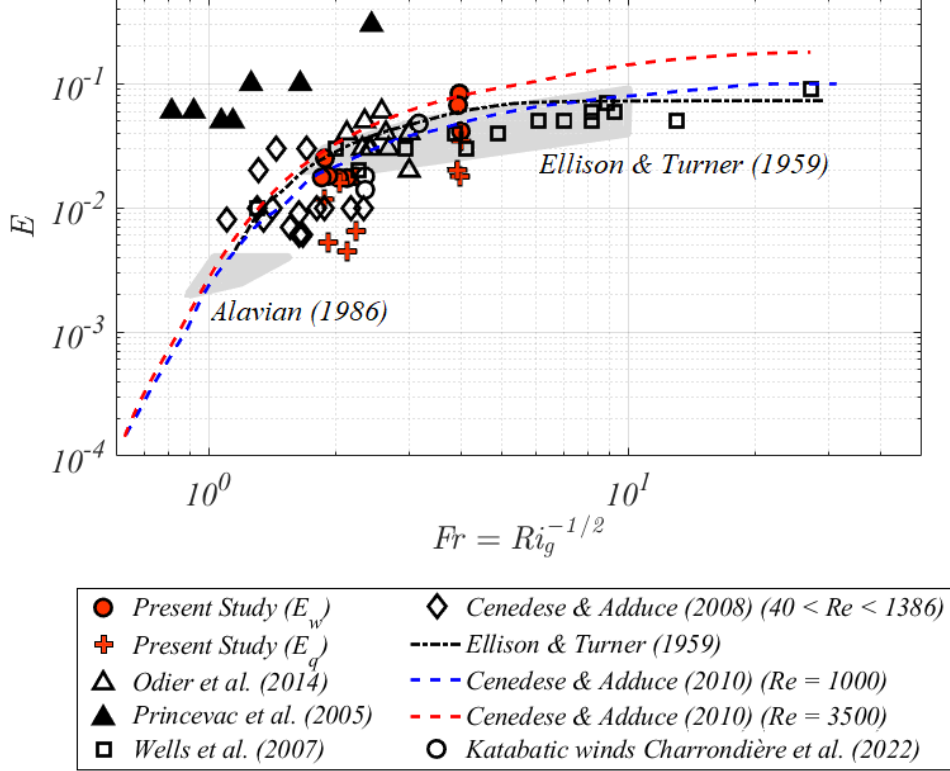


FIG. 6. Entrainment coefficients, E_w (red \circ), and E_q (red $+$) as a function of the local Froude number $Fr = Ri_g^{-1/2}$. Present entrainment coefficients are for the range $0.5 < x^* < 1.5$, $6.5 < x^* < 7.5$ and $10.5 < x^* < 11.5$ of all experiments with $g'_0 = 5 \text{ cm s}^{-2}$. Data of E_w from Odier, Chen, and Ecke³⁶, Princevac, Fernando, and Whiteman⁵⁴, Wells, Cenedese, and Caulfield⁵⁵, Cenedese and Adduce⁵⁶ and Charrondière *et al.*⁶ (katabatic winds in situ measurements) are included for comparison. Shaded areas represent laboratory experiments of Alavian⁵⁷ and Ellison and Turner²⁶ with the black dashed line representing the classical variation of Ellison and Turner²⁶ and the dashed blue and red lines the variation as reported in Cenedese and Adduce⁵⁸.

183 In experiment $R5_2$ the profile above maximum velocity is similar to that of a mixing layer
 184 i.e. of erf type⁶², whereas when g'_0 is larger, higher acceleration due to larger gravitational
 185 force, gives rise to a wider region of nearly constant shear and consequently constant normal
 186 stresses. Stratification has practically no effect on Reynolds stresses at $x^* = 7$, the gradient
 187 Richardson number being small (of order 0.1). At $x^* = 11$ a region of nearly constant
 188 shear exists in all three experiments, hence nearly constant normal stresses over this region.

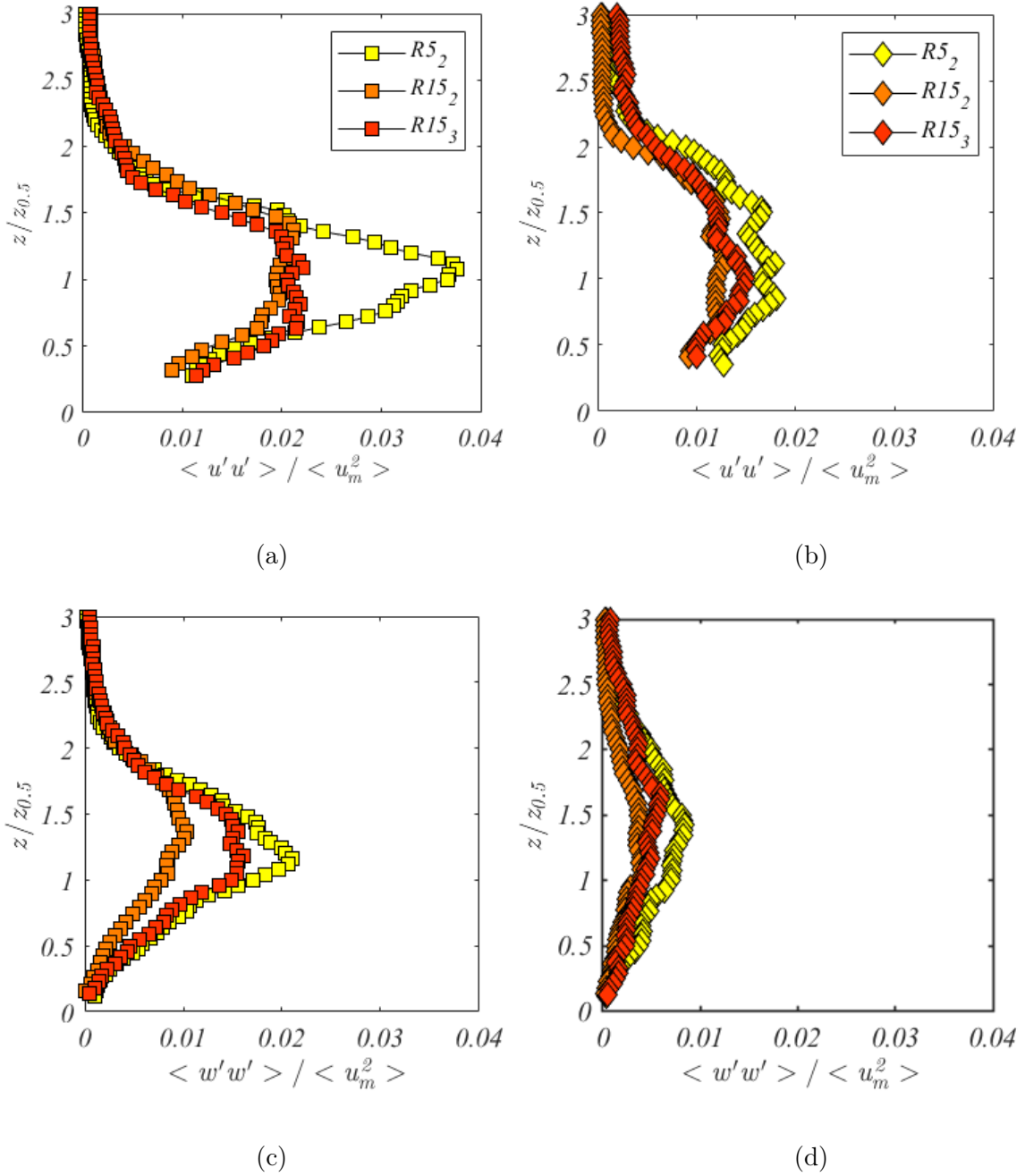


FIG. 7. Scaled normal Reynolds stress profiles determined at $x^* = 7$ (a,c) and $x^* = 11$ (b,d) in experiments $R5_2$, $R15_2$ and $R15_3$.

189 Maximum values of the Reynolds stresses are about half of those at $x^* = 7$ due to the
 190 collapse of KHIs and re-stratification process that takes place at the end of the slope.

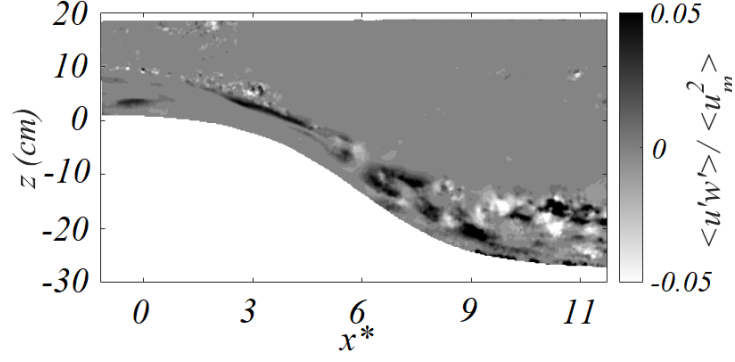
192 The Reynolds shear stresses $\langle u'w' \rangle$ are shown in Fig. 8, with the instantaneous two-
 193 dimensional field of the scaled Reynolds shear stresses $\langle u'w' \rangle$ along x^* , of experiment $R5_2$,

194 presented in Fig. 8a. As previously observed³³, in the HI region the largest fluctuations
 195 are concentrated at the sheared interface only. As the current develops down the slope, an
 196 increase of the shear stresses is observed due to acceleration and rapid onset of the KHI,
 197 which spread over the full current depth: large values of $\langle u'w' \rangle / \langle u_m^2 \rangle$ characterize the full
 198 shear layer with the largest values on the steepest part of the slope at $x^* = 7$ where $\theta = 31^\circ$.
 199 This is highlighted in Fig.8b and Fig.8c where scaled Reynolds shear stress profiles, computed
 200 at $x^* = 7$ and $x^* = 11$, respectively, are reported. In accordance with the behaviour of the
 201 normal stresses, at $x^* = 7$ there is a clear maximum in experiment $R5_2$, located at the
 202 sheared interface close to $z/z_{0.5} = 1$ whereas when g'_0 is larger, maximum values are lower
 203 and spread out. Furthermore, at $x^* = 11$ where there is a general decrease of the turbulent
 204 fluctuations, the shear stress values are less than half of those at $x^* = 7$.

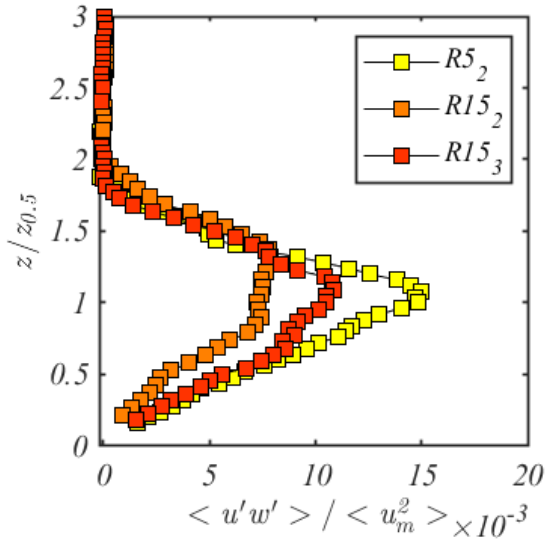
206 Odier, Chen, and Ecke⁴⁷ proposed a novel method for characterizing the distribution of
 207 correlations of the velocity fluctuations to better understand the mixing process based on the
 208 probability density functions (PDFs) of the momentum fluxes $\langle u'w' \rangle$. Fig.9 shows the PDFs
 209 of $\langle u'w' \rangle$ in the range $8.5 < x^* < 11.5$ of experiment $R15_2$. Each PDF is obtained using data
 210 in a normal band of $1cm$ height, starting from the bottom of the slope, and is highlighted
 211 with a different color enabling to see the evolution of the PDFs as the vertical distance
 212 increases. As also seen in Fig. 8, the fluxes reach nearly 2% of the squared maximum
 213 velocity flow so as there is still a probability (10^{-3}) that a fluctuation will reach a value
 214 about 15 times the mean (Fig.9). Usually, as the center of the mixing region is approached,
 215 i.e. the interface between the current and the ambient fluid, large fluctuations are present
 216 and the PDFs of the momentum fluxes are asymmetric⁴⁷. This asymmetry is the origin of
 217 the non-zero mean value of the fluxes indicating either downward transport (entrainment)
 218 of downstream momentum or upward transport of upstream momentum, according to the
 219 mixing mechanism induced by the KHI. This behavior is not observed in our analysis, since
 220 the PDF were evaluated on the TSL area where the stratification is interrupted by the
 221 collapse of the KHIs.

223 C. Mixing length and shear scale

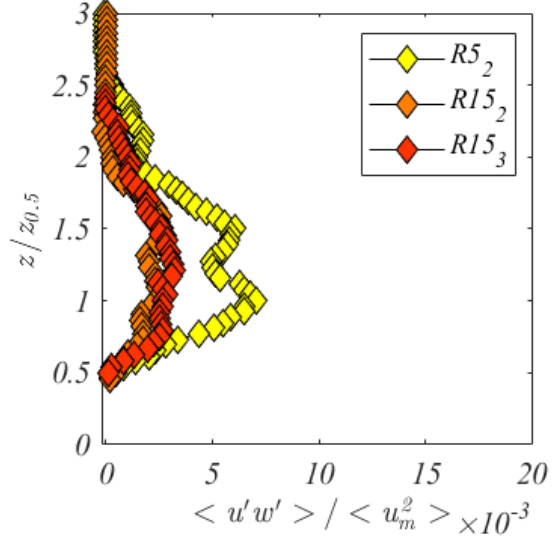
224 Reynolds stresses can be conceptually parameterised by an eddy or turbulent viscosity,
 225 $K_m = -\langle u'w' \rangle / \partial_z u$, that relates chaotic fluid motion to diffusive type processes^{43,62}. It is a



(a)



(b)

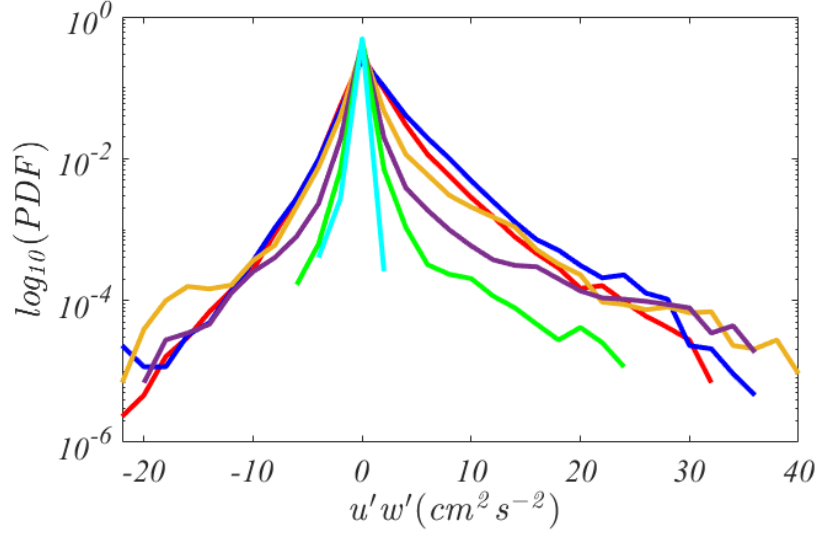


(c)

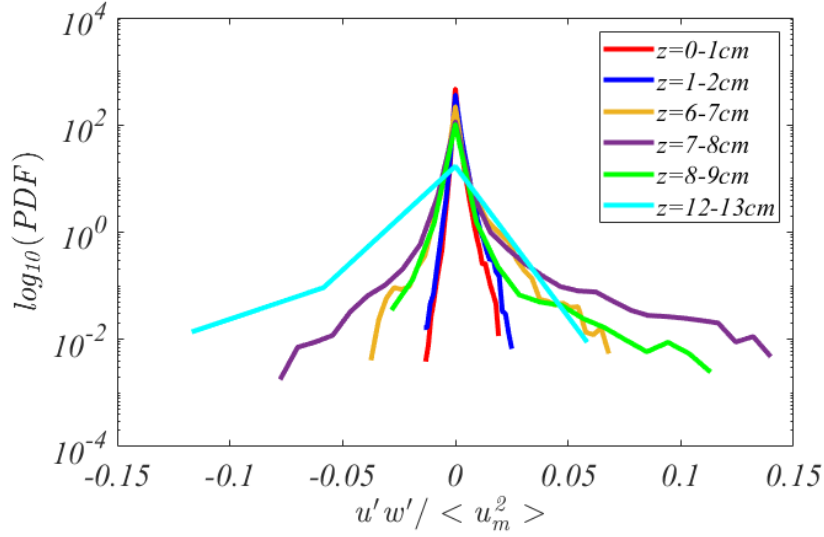
FIG. 8. (a) Scaled instantaneous Reynolds shear stresses $\langle u'w' \rangle / \langle u_m^2 \rangle$ along x^* of experiment $R5_2$. Profiles of scaled Reynolds shear stresses at $x^* = 7$ (b) and at $x^* = 11$ (c) in experiments $R5_2$, $R15_2$ and $R15_3$.

226 useful parameter for indicating the extent of internal mixing and is used extensively in both
 227 numerical and analytical modelling of turbulent flows.

228 Based on the mixing length model proposed by Prandtl⁶³, the Reynolds stresses $\langle u'w' \rangle$
 229 can also be related to the square of the velocity gradient $\langle \partial_z u \rangle^2$ using a proportionality
 230 constant which represents a mixing length L_m :



(a)



(b)

FIG. 9. PDFs of instantaneous shear stress (a), and of scaled shear stress (b) in $R15_2$ experiment. Each PDF is constructed using data in a band of 1cm height from the bottom (normal position indicated in the legend), situated in the TSL area at $8.5 < x^* < 11.5$.

$$L_m^2 = \frac{\langle u'w' \rangle}{\langle \partial_z u \rangle^2}, \quad (3)$$

231

232 Fig.10 shows the computed vertical profiles of the turbulent eddy diffusivity K_m (a,b)

233 and mixing lengths L_m (c,d) at $x^* = 7$ and $x^* = 11$ (left and right columns, respectively).

234 The corresponding z variation of mean velocity gradients $\partial_z u$ are presented in the insets.
 235 Data close to the bottom and top extremities are not reported because experimental errors
 236 become large. L_m is computed starting at a distance from the wall of approximately 20% of
 237 the current depth⁶².

238 At $x^* = 7$ (Fig.10c), mixing lengths L_m are nearly constant in experiments $R15_2$ and
 239 $R15_3$. while eddy coefficients increase and then decrease with distance z . When density
 240 differences are lower ($R5_2$), both, L_m and K_m behave differently in the lower part because
 241 of the difference in velocity gradient. In general, close to the velocity maximum and at large
 242 distances from the bottom, the vertical derivative $\partial_z u$ becomes almost zero, so that large
 243 fluctuations in the calculated L_m occur at these extremities. Averaging over the depth and
 244 the downstream distance in the considered region, gives a mean value of $L_m \approx 0.60 \pm 0.1$,
 245 which compares well with those reported by Odier *et al.*⁴⁰ of $L_m \approx 0.45 \pm 0.1$.

246 At the end of the slope in the TSL region ($x^* = 11$) (Fig.10b) the values of L_m and of
 247 K_m are lower and both increase almost linearly with $z/z_{0.5}$. This is probably related with
 248 the substantially lower and nearly constant Reynolds stresses at this location.

249 In order to understand how mixing lengths and eddy coefficients depend on the effect of
 250 turbulent kinetic energy, of stable stratification, and of destabilization by shear it is useful
 251 to determine the shear scale L_s , also referred to as Corrsin scale⁶⁴, and the buoyancy length
 252 (Ozmidov scale) L_o , which are defined as^{36,65}:

$$253 \quad L_s = \sqrt{\frac{\bar{\epsilon}}{\langle \partial_z u \rangle^3}}, \quad L_o = \sqrt{\frac{\bar{\epsilon}}{\left(g \frac{\langle \partial_z \rho \rangle}{\langle \bar{\rho} \rangle}\right)^{3/2}}}, \quad (4)$$

254 where $\overline{\langle \cdot \rangle}$ represents a time average over the experimental duration and $\bar{\epsilon}$ the mean turbulent
 255 dissipation rate. As already pointed out by Odier, Chen, and Ecke⁴⁷, the smaller of these
 256 scales limits the mixing length L_m , hence, also K_m . The strength of stratification with
 257 respect to the shear is measured by the (gradient) Richardson number Ri_g which also relates
 258 these two scales via the relation $L_s/L_o = Ri_g^{3/2}$. Generally, gravity currents on slopes are
 259 characterized by low Richardson numbers $Ri_g \ll 1$, hence shear dominates over stratification
 260 so that the shear scale L_s is expected to limit the mixing length L_m and K_m .

261 According to Kolmogorov's similarity hypothesis, the dissipation is the only flow variable
 262 that characterizes the state of turbulence when stratification is weak. The significance of
 263 ϵ has been extensively addressed in numerous studies^{66–68}. Following Steinbuck *et al.*⁶⁹

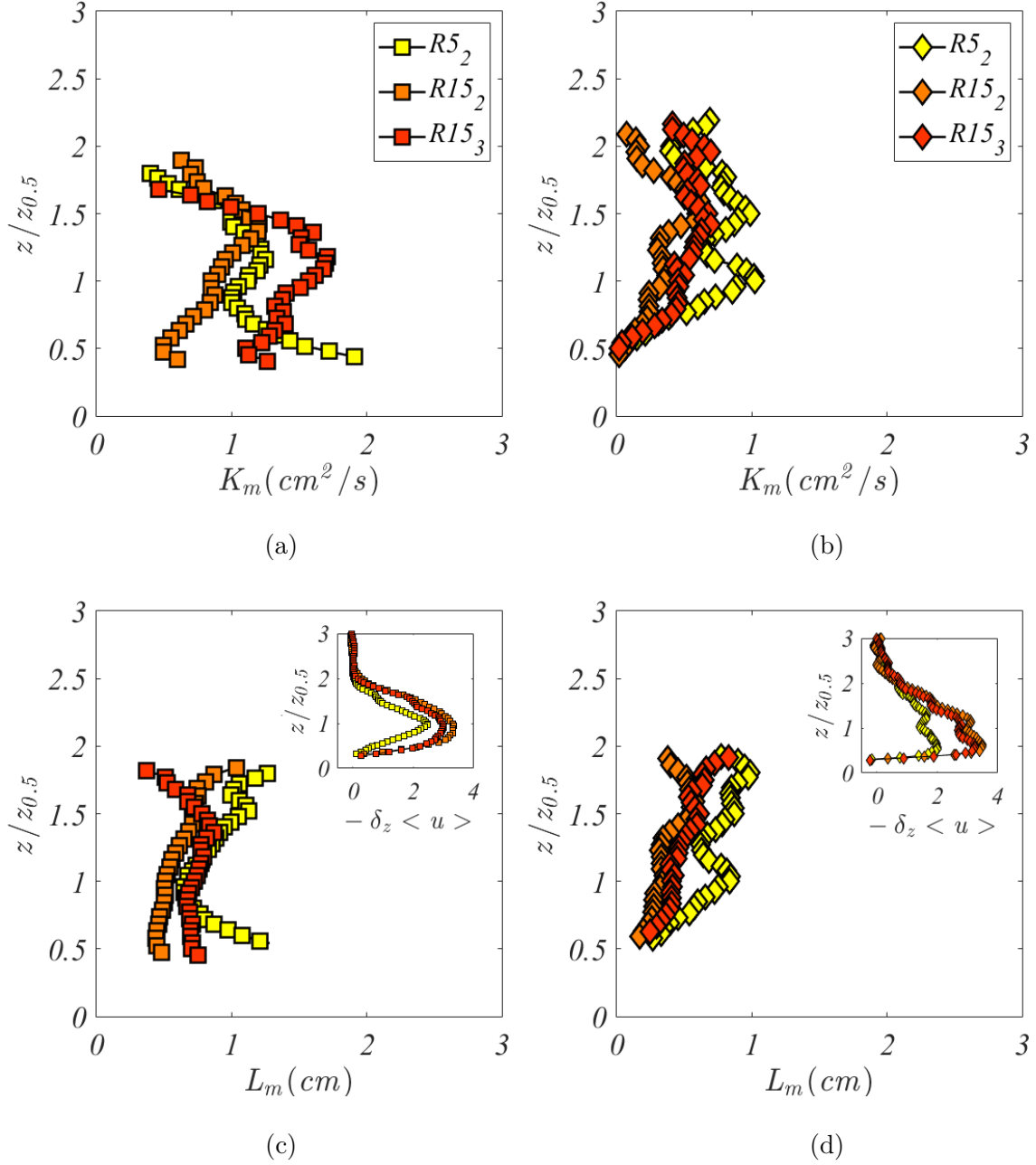


FIG. 10. Variations of eddy coefficient K_m and mixing lengths L_m with $z/z_{0.5}$ at $x^* = 7$, (a,c) and at $x^* = 11$, (b,d). Close to the velocity maximum, as well as far away from it, the $\partial_z u$ tend to vanish, producing large fluctuations in K_m and L_m . The insets show the velocity gradients $\partial_z u$ as a function of $z/z_{0.5}$.

264 and Xu and Chen⁶⁸ the dissipation rate can be estimated using the four resolved velocity
 265 gradients obtained by PIV as:

266
$$\epsilon = \nu \langle 4(\partial_x u')^2 + 4(\partial_z w')^2 + 3(\partial_z u')^2 + 3(\partial_x w')^2 + 4(\partial_x u' \partial_z w') + 6(\partial_z u' \partial_x w') \rangle \quad (5)$$

267 In a stratified flow the dissipation is equal to production minus the loss of energy to
 268 buoyancy. In a flow on a slope there is, in addition to shear production, also TKE production
 269 by buoyancy. Neglecting advection and diffusion terms, the TKE energy balance is given
 270 by:

$$271 \quad -\overline{u'w'}\frac{\partial u}{\partial z} - \frac{g}{\rho}\overline{w'\rho'}\cos\theta + \frac{g}{\rho}\overline{u'\rho'}\sin\theta \approx \epsilon \quad (6)$$

272 The buoyancy terms are opposite in sign with the ratio of $\frac{g}{\rho}\overline{w'\rho'}\cos\theta$ to shear and
 273 buoyancy production (mixing efficiency) being ≈ 0.1 and $\overline{u'\rho'}\sin\theta / \overline{w'\rho'}\cos\theta \leq 1$ when
 274 $Ri_g < 0.1^6$; hence $\epsilon \approx \overline{w'u'}\partial_z u$. The production is maximum near $z/z_{0.5}$ whereas, because
 275 of diffusion and advection terms, dissipation is more uniformly distributed across the outer
 276 region of the current and is close to the average of the production, i.e.:

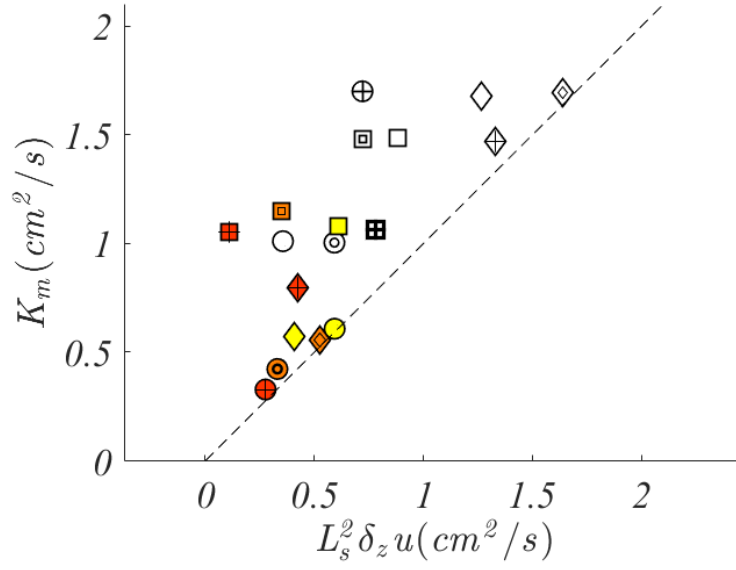
$$277 \quad \bar{\epsilon} \approx 0.6(\overline{w'u'\partial_z u})_{max}. \quad (7)$$

278 The value of ϵ computed from equation (5) is nearly up to an order of magnitude less than $\bar{\epsilon}$
 279 from equation (7). To estimate the dissipation rate ϵ directly from the PIV data and avoid
 280 important underestimations, it is necessary to have a spatial resolution of the PIV close to
 281 the Kolmogorov scale η_K . The spatial resolution of the present PIV measurements is $3mm$,
 282 while $\eta_K = (\nu^3/\epsilon)^{1/4}$ is of the order of $\mathcal{O} \sim 0.4mm$ estimated using $\epsilon = u'^3/h^{70}$. Hence the
 283 direct calculation of ϵ from the PIV data using equation (5) will considerably underestimate
 284 the dissipation. To calculate the values of L_s we use the z variation given by equation (5)
 285 with a pre-factor such that the maximum of ϵ is close to $\bar{\epsilon}$ of equation (7).

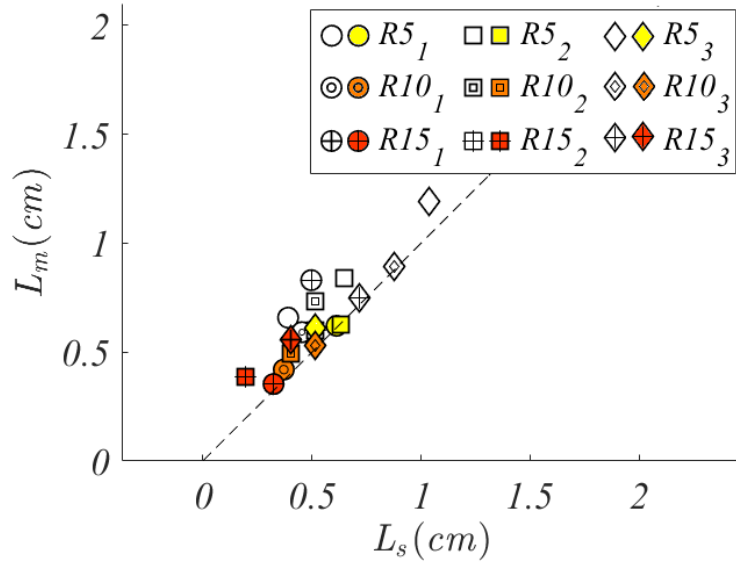
286 Fig.11 shows the measured mixing length L_m versus the computed shear scale L_s and
 287 K_m versus $L_s^2\delta_z u$ for all the experiments performed. The experimental data of the present
 288 study all are close to or fall above the dashed straight line in Fig.11 representing $L_m = L_s$
 289 $K_m = L_s^2\delta_z u$, which is different from the results of Odier, Chen, and Ecke⁴⁷ where $L_m < L_s$.
 290 A possible explanation for the difference is the non-constant and much steeper bottom slope
 291 θ in the present experiments that can have important consequences on the mixing properties.

292 IV. COMPARISON WITH KATABATIC WINDS

293 Studies of katabatic winds are numerous (see for instance^{4,6}) because these flows affect
 294 local weather conditions causing also temperature inversion in valleys that are prone to
 295 pollution. In Antarctica and Greenland, katabatic winds are directly responsible for cooling



(a)



(b)

FIG. 11. Eddy coefficient K_m versus $L_s^2 \delta_z u$ and mixing length L_m versus computed shear length L_s , for all the experiments performed at $x^* = 7$ (empty markers) and $x^* = 11$ (filled markers).

296 the ocean surface water at the polynya⁷¹ and open sea and play an important role for the deep
 297 water formation. Katabatic flows are driven by buoyancy supply from the ground (ground

TABLE II. Characteristic turbulence length scales of present experiments of Odier, Chen, and Ecke⁴⁷ and in katabatic flows¹. The dissipation ϵ has been computed using equations (5) and (7). $\Delta z = \Delta u / \partial_z u_{z_{0.5}}$ is the shear thickness.

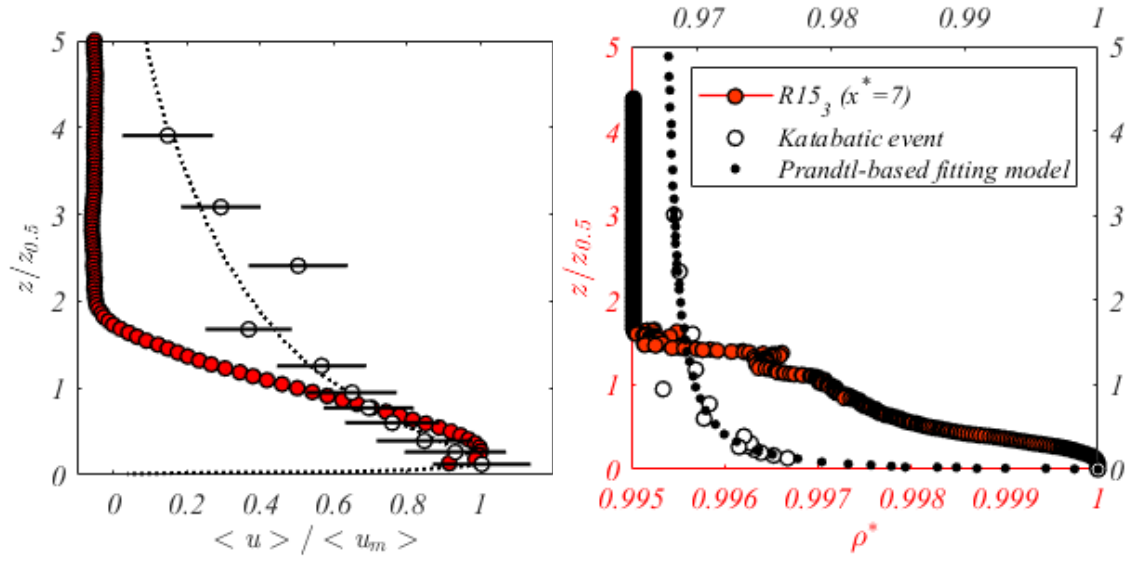
Run	$\langle \epsilon \rangle (\text{cm}^2 \text{s}^{-3})$	$L_m (\text{cm})$	$L_s (\text{cm})$	$ \Delta z (\text{cm})$	$z_{0.5} (\text{cm})$
$R15_2(x^* = 7)$	6.8	0.61	0.51	6.0	6.8
$R15_2(x^* = 11)$	1.0	0.38	0.20	7.5	5.6
$R15_3(x^* = 7)$	9.0	0.75	0.72	7.0	8.0
$R15_3(x^* = 11)$	2.8	0.55	0.40	9.9	5.9
Charrondière, Hopfinger, and Brun ¹					
$z = 0.66\text{m}$	57	9	21	$11.1 \cdot 10^2$	$3.7 \cdot 10^2$
$z = 0.98\text{m}$	55	16	21	$11.1 \cdot 10^2$	$3.7 \cdot 10^2$
$z = 1.50\text{m}$	52	26	27	$11.1 \cdot 10^2$	$3.7 \cdot 10^2$
$z = 1.93\text{m}$	44	35	32	$11.1 \cdot 10^2$	$3.7 \cdot 10^2$
$z = 2.37\text{m}$	40	45	39	$11.1 \cdot 10^2$	$3.7 \cdot 10^2$
$z = 9.77\text{m}$	46	116	120	$11.1 \cdot 10^2$	$3.7 \cdot 10^2$
Odier, Chen, and Ecke ⁴⁷					
	$0.5 \div 1.4$	$0.2 \div 0.6$	$0.15 \div 0.7$	$1.6 \div 6.8$	

298 cooling), whereas in most laboratory currents buoyancy flux is constant and equal to the
 299 upstream buoyancy supply, hence, the flow structure is expected to be different. A formal
 300 comparison is, nevertheless, of interest. Ellison and Turner²⁶ for instance evaluated the mean
 301 flow development of katabatic winds using their results of a buoyancy conserving gravity
 302 current on a slope. The recent detailed field measurements by Charrondière *et al.*^{6,46,72} on
 303 steep alpine slopes of 30° inclination (Grand Colon, Belledonne chain) provide an excellent
 304 data set for comparing katabatic jets data, including turbulent mixing, with laboratory
 305 gravity currents results. The shape and slope inclination adopted in the present study
 306 reproduces a typical alpine topography in the French Alps and specifically the Grand Colon
 307 topography.

309 Fig.12a shows a comparison of the slope normal katabatic wind mean velocity profile dur-
 310 ing a representative katabatic event on February 24th 2019 (5h-8h) with a slight up-slope
 311 wind of velocity $U_a = -0.2\text{m/s}$, with the $R15_3$ experimental mean velocity. The errors

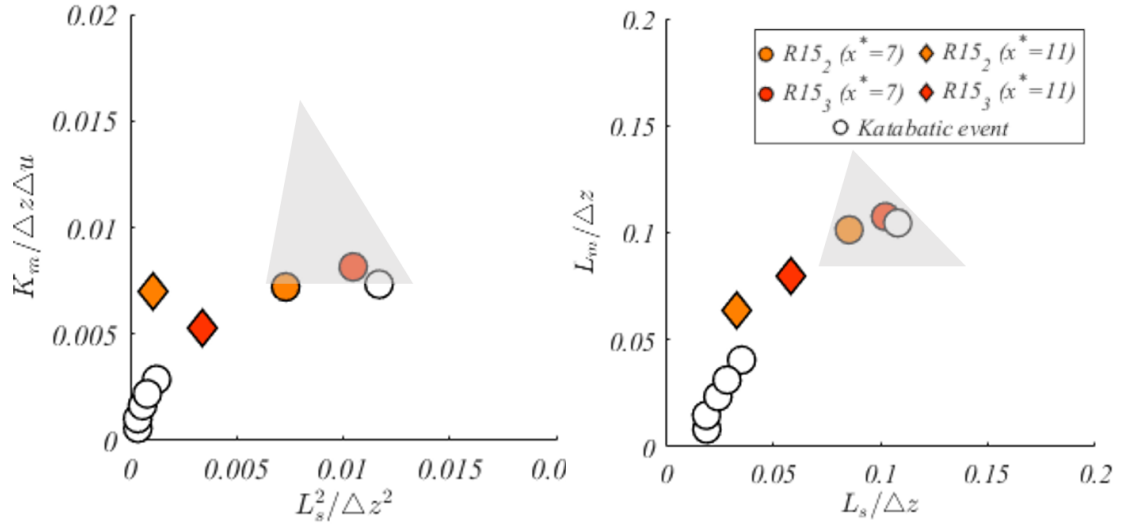
312 bars on the katabatic velocity profile show the variability of the mean wind during the kata-
 313 batic event, while the black dashed line represents the fit derived from the Prandtl model⁵.
 314 The velocity profiles are quite different: indeed in katabatic winds the velocity distribution
 315 above maximum velocity has a logarithmic trend with maximum gradient close to the ve-
 316 locity maximum whereas in laboratory experiments the maximum gradient is located near
 317 the current mid-height. The explanation for this difference are the very different density
 318 distributions, as presented in Fig.12b. In the constant, upstream buoyancy supply of labo-
 319 ratory gravity currents, the excess density decreases over the whole flow depth, whereas in
 320 the katabatic wind (buoyancy supply from the boundary) the density variation is located in
 321 the lower 10 – 20% of the gravity flow. In spite of this considerable difference in mean flow,
 322 in addition to the large difference in Reynolds number, entrainment coefficients lie within
 323 the bulk of laboratory currents as is seen in Fig.6.

324 To compare turbulence quantities, notably mixing lengths L_m and K_m , with those ob-
 325 tained in katabatic winds, extended to larger z values given in Charrondière, Hopfinger, and
 326 Brun¹ (cf. Tab.II), a characteristic length scale is required for making L_m , K_m as well as L_s
 327 dimensionless. An appropriate length scale is $\Delta z = \Delta u / \partial_z u_{z_{0.5}}$, where Δu is the maximum
 328 mean velocity u_m . Indeed, by adopting the latter, all the data collapses reasonably well
 329 as is shown in Figs.12(c,d), where in (c), $K_m / \Delta z \Delta u$ are plotted as a function of $L_s^2 / \Delta u^2$
 330 and in (d), mixing lengths $L_m / \Delta z$ as a function of $L_s / \Delta z$. Both, the scaled K_m and L_m
 331 increase with L_s to reach an upper limit of $K_m / \Delta z \Delta u \approx 0.008$ and $L_m / \Delta z \approx 0.1$. Inter-
 332 estingly, these maximum values of dimensionless eddy coefficients and mixing lengths are
 333 similar to that of a turbulent boundary layer where $L_m / \delta \approx 0.1$ (the shear thickness Δz is
 334 the equivalent of the velocity shear layer thickness δ). In terms of bottom friction velocity,
 335 $u_\tau \approx 0.07 u_m$ ⁶, $K_m / \Delta z u_\tau \approx 0.1$, and which is close to the maximum value in a turbulent
 336 boundary layer (Pope⁶², p.307). However, the variations of eddy coefficients and mixing
 337 lengths with L_s , have quite different origins. In katabatic flows, these are a function of
 338 height z with values increasing from nearly zero up to the maximum value, whereas in the
 339 constant buoyancy flux gravity current, the mixing length is practically constant along z .
 340 The change seen in Figs.12(c,d) is due to a change with position x , i.e. values are maximum
 341 at $x^* = 7$ and lower at $x^* = 11$. The eddy coefficient varies with z and with x . This notable
 342 difference with katabatic winds is due to the widely different mean velocity profiles.



(a)

(b)



(c)

(d)

FIG. 12. Dimensionless profiles of mean streamwise velocity, (a) and of density, (b), at $x^* = 7$ in experiment $R15_3$ compared with katabatic wind profiles of 2019B event in⁶. Dimensionless eddy coefficients K_m , (c), and mixing lengths L_m (d), versus dimensionless shear length L_s . The shaded gray area represents the values of Odier, Chen, and Ecke⁴⁷.

344 V. SUMMARY AND CONCLUDING REMARKS

345 The constant buoyancy flux gravity currents flowing from horizontal onto a steep, hy-
346 perbolic tangent shaped slope that is representative of an alpine topography, reveal novel
347 features. The current accelerates down the slope until Kelvin-Helmholtz instabilities de-
348 velop, which cause the slow down of the current followed by a nearby maximum constant
349 velocity. Downstream the slope, on the horizontal boundary, the maximum velocity remains
350 nearly unchanged because both the gravitational force and entrainment are drastically re-
351 duced. The interfacial instability changes from Holmboe instability (HI) near slope begin to
352 Kelvin-Helmholtz (KHI) on the steepest part of the slope, where $Ri_g \approx 0.1$ and entrainment
353 is large, followed by turbulence collapse, i.e. a stable turbulent shear layer (TSL), where
354 $Ri_g \approx 0.3$ and entrainment ceases.

355 The computed Reynolds stresses are maximum in the central part of the interface with
356 the distribution depending on the buoyancy flux. In the TSL region Reynolds stresses are
357 more spread out. Mixing lengths determined via the correlation terms between fluctuating
358 components of the velocity field at the location of the steepest slope ($x^* = 7$) and at
359 a downstream position in the turbulent shear layer (TSL) region ($x^* = 11$) are practically
360 constant across the shear zone whereas eddy coefficients vary with height. Both scale closely
361 with the shear scale, in agreement with Odier, Chen, and Ecke⁴⁷. The comparison between
362 the present saline gravity current experiments and of field data, obtained in katabatic winds
363 on alpine slopes, highlights the very different mean flow structures. However, the mixing
364 lengths and the eddy coefficients data agree surprisingly well and collapse when using an
365 appropriate scaling which has been defined as $(\Delta z = \Delta u / \partial_z u_{z_{0.5}})$, even though Reynolds
366 numbers between the laboratory and the observational data differ at least of two orders of
367 magnitude. An upper limit of mixing length and eddy coefficient is reached at a certain
368 value of the shear scale, corresponding to a certain height in katabatic winds.

369 Reproducing katabatic wind conditions in the laboratory would be of interest for the
370 understanding of certain important aspects of these flows. It is for instance well documented
371 that katabatic winds exhibit mean flow oscillations^{4,6,73} and it has been speculated that these
372 oscillations are related with ambient stratification. Thus, experiments with saline gravity
373 currents in the presence of ambient stratification could help in clarifying the underlying
374 mechanism of these oscillations. As a further step, simulating katabatic flow conditions

375 in the laboratory, by injecting a saline solution through a porous bottom boundary or by
376 cooling it, would allow to study the spatial mean flow development and related mixing
377 characteristics proper of katabatic flows.

378 **ACKNOWLEDGEMENTS**

379 The authors are very grateful to Claudine Charrondiere for making available the katabatic
380 wind in situ data and for fruitful discussions. Special thanks go to Joseph Virone and Vincent
381 Govart for their technical support in preparing the experiments. Financial support was given
382 by a grant from Labex OSUG@2020 (Investissements d’avenir ANR10 LABX56).

383 **DECLARATION OF INTERESTS**

384 The authors report no conflict of interest.

385 **AUTHOR STATEMENT**

386 We hereby declare and confirm that all the authors have substantially contributed to the
387 work, and have read and approved the submitted manuscript.

388 **DATA AVAILABILITY STATEMENT**

389 The data that support the findings of this study are available from the corresponding
390 author upon reasonable request.

391 **REFERENCES**

- 392 ¹C. Charrondière, E. J. Hopfinger, and C. Brun, “Identification of k_x^{-1} strong wave tur-
393 bulence and of $k_x^{-7/5}$ temperature spectral ranges in katabatic winds on a steep slope,”
394 Journal of Fluid Mechanics. (Accepted).
- 395 ²J. E. Simpson, *Gravity currents: In the environment and the laboratory* (Cambridge Uni-
396 versity Press, 1997).

- 397 ³H. Fernando, “Fluid dynamics of urban atmospheres in complex terrain,” *Annu. Rev. Fluid*
398 *Mech.* **42**, 365–389 (2010).
- 399 ⁴M. Princevac, J. C. R. Hunt, and H. J. S. Fernando, “Quasi-steady katabatic winds on
400 slopes in wide valleys: Hydraulic theory and observations,” *J. of Atm. Sci.* **65**, 627 – 643
401 (2008).
- 402 ⁵C. Brun, S. Blein, and J.-P. Chollet, “Large-eddy simulation of a katabatic jet along a
403 convexly curved slope. part i: Statistical results,” *Journal of the Atmospheric Sciences* **74**,
404 4047–4073 (2017).
- 405 ⁶C. Charrondière, C. Brun, E. J. Hopfinger, J.-M. Cohard, and J.-E. Sicart, “Mean flow
406 structure of katabatic winds and turbulent mixing properties,” *Journal of Fluid Mechanics*
407 **941** (2022).
- 408 ⁷A. L. Gordon, A. H. Orsi, R. Muench, B. A. Huber, E. Zambianchi, and M. Visbeck,
409 “Western ross sea continental slope gravity currents,” *Deep Sea Research Part II: Topical*
410 *Studies in Oceanography* **56**, 796–817 (2009).
- 411 ⁸E. Meiburg and B. Keller, “Turbidity currents and their deposits,” *Annu. Rev. Fluid Mech.*
412 **42**, 135–156 (2010).
- 413 ⁹E. Hopfinger, “Snow avalanche motion and related phenomena,” *Annu. Rev. Fluid Mech.*
414 **15**, 47–76 (1983).
- 415 ¹⁰B. Marino, L. Thomas, and P. Linden, “The front condition for gravity currents,” *J. Fluid*
416 *Mech.* **536**, 49–78 (2005).
- 417 ¹¹M. E. Negretti, D. Z. Zhu, and G. H. Jirka, “Barotropically induced interfacial waves in
418 two-layer exchange flows over a sill,” *Journal of Fluid Mechanics* **592**, 135–154 (2007).
- 419 ¹²H. I. Nogueira, C. Adduce, E. Alves, and M. J. Franca, “Analysis of lock-exchange gravity
420 currents over smooth and rough beds,” *J. Hydraul. Res.* **51**, 417–431 (2013).
- 421 ¹³R. Inghilesi, C. Adduce, V. Lombardi, F. Roman, and V. Armenio, “Axisymmetric three-
422 dimensional gravity currents generated by lock exchange,” *J. Fluid Mech.* **851**, 507–544
423 (2018).
- 424 ¹⁴M. C. De Falco, C. Adduce, A. Cuthbertson, M. E. Negretti, J. Laanearu, D. Malcangio,
425 and J. Sommeria, “Experimental study of uni-and bi-directional exchange flows in a large-
426 scale rotating trapezoidal channel,” *Phys. Fluids* **33**, 036602 (2021).
- 427 ¹⁵M. La Rocca, P. Prestininzi, C. Adduce, G. Sciortino, R. Hinkelmann, *et al.*, “Lattice
428 boltzmann simulation of 3d gravity currents around obstacles,” *Int. J. Offshore Polar*

- 429 Engineering **23** (2013).
- 430 ¹⁶A. Cuthbertson, J. Laanearu, M. Carr, J. Sommeria, and S. Viboud, “Blockage of saline
431 intrusions in restricted, two-layer exchange flows across a submerged sill obstruction,”
432 Environmental Fluid Mechanics **18**, 27–57 (2018).
- 433 ¹⁷Venuleo, Sara and Pokrajac, Dubravka and Schleiss, Anton J and Franca, Mário J,
434 “Continuously-fed gravity currents propagating over a finite porous substrate,” Phys. Flu-
435 ids **31**, 126601 (2019).
- 436 ¹⁸Zhou, Jian and Venayagamoorthy, Subhas K, “How does three-dimensional canopy ge-
437 ometry affect the front propagation of a gravity current?” Physics of Fluids **32**, 096605
438 (2020).
- 439 ¹⁹M. De Falco, C. Adduce, and M. Maggi, “Gravity currents interacting with a bottom
440 triangular obstacle and implications on entrainment,” Advances in Water Resources **154**,
441 103967 (2021).
- 442 ²⁰M. R. Maggi, C. Adduce, and M. E. Negretti, “Lock-release gravity currents propagating
443 over roughness elements,” Environmental Fluid Mechanics , 1–20 (2022).
- 444 ²¹C. Adduce, M. R. Maggi, and M. C. De Falco, “Non-intrusive density measurements in
445 gravity currents interacting with an obstacle,” Acta Geophysica , 1–12 (2022).
- 446 ²²He, Zhiguo and Han, Dongrui and Lin, Ying-Tien and Zhu, Rui and Yuan, Yeping and
447 Jiao, Pengcheng, “Propagation, mixing, and turbulence characteristics of saline and tur-
448 bidity currents over rough and permeable/impermeable beds,” Physics of Fluids **34**, 066604
449 (2022).
- 450 ²³P. G. Baines, “Mixing regimes for the flow of dense fluid down slopes into stratified envi-
451 ronments,” Journal of Fluid mechanics **538**, 245–267 (2005).
- 452 ²⁴A. Dai, “Non-boussinesq gravity currents propagating on different bottom slopes,” Journal
453 of Fluid Mechanics **741**, 658–680 (2014).
- 454 ²⁵T. Zemach, M. Ungarish, A. Martin, and M.-E. Negretti, “On gravity currents of fixed
455 volume that encounter a down-slope or up-slope bottom,” Physics of Fluids **31**, 096604
456 (2019).
- 457 ²⁶T. Ellison and J. Turner, “Turbulent entrainment in stratified flows,” J. Fluid Mech. **6**,
458 423–448 (1959).
- 459 ²⁷G. Pawlak and L. Armi, “Mixing and entrainment in developing stratified currents,” Jour-
460 nal of Fluid Mechanics **424**, 45–73 (2000).

- 461 ²⁸M. C. De Falco, L. Ottolenghi, and C. Adduce, “Dynamics of gravity currents flowing up
462 a slope and implications for entrainment,” *J. Hydraul. Eng.* **146**, 04020011 (2020).
- 463 ²⁹M. C. De Falco, C. Adduce, M. E. Negretti, and E. J. Hopfinger, “On the dynamics of
464 quasi-steady gravity currents flowing up a slope,” *Adv. Water Res.* **147**, 103791 (2021).
- 465 ³⁰Marshall, CR and Dorrell, RM and Dutta, S and Keevil, GM and Peakall, J and Tobias,
466 SM, “The effect of Schmidt number on gravity current flows: The formation of large-scale
467 three-dimensional structures,” *Physics of Fluids* **33**, 106601 (2021).
- 468 ³¹Nicholson, Mitchell and Flynn, Morris R, “Gravity current flow over sinusoidal topography
469 in a two-layer ambient,” *Physics of Fluids* **27**, 096603 (2015).
- 470 ³²M. Negretti, J. Flòr, and E. Hopfinger, “Development of gravity currents on rapidly
471 changing slopes,” *J. Fluid Mech.* **833**, 70–97 (2017).
- 472 ³³A. Martin, M. E. Negretti, and E. J. Hopfinger, “Development of gravity currents on
473 slopes under different interfacial instability conditions,” *Journal of Fluid Mechanics* **880**,
474 180–208 (2019).
- 475 ³⁴M. Negretti, A. Martin, and F. Naaim Bouvet, “On the propagation of the front speed of
476 lock released density clouds,” *Adv. Water Res.* (2022).
- 477 ³⁵H. J. Fernando, “Turbulent mixing in stratified fluids,” *Annual review of fluid mechanics*
478 **23**, 455–493 (1991).
- 479 ³⁶P. Odier, J. Chen, and R. E. Ecke, “Entrainment and mixing in a laboratory model of
480 oceanic overflow,” *Journal of Fluid Mechanics* **746**, 498–535 (2014).
- 481 ³⁷W. D. Smyth, J. R. Carpenter, and G. A. Lawrence, “Mixing in symmetric holmboe
482 waves,” *Journal of Physical Oceanography* **37**, 1566 – 1583 (2007).
- 483 ³⁸N. Laanaia, A. Wirth, J.-M. Molines, B. Barnier, and J. Verron, “On the numerical
484 resolution of the bottom layer in simulations of oceanic gravity currents,” *Ocean Sci.* **6**,
485 563–572 (2010).
- 486 ³⁹G. Danabasoglu, W. Large, and B. Briegleb, “Climate impacts of parametrized nordic sea
487 overflows,” *J. Geophys. Res.* **115**, C11005 (2010).
- 488 ⁴⁰P. Odier, J. Chen, M. K. Rivera, and R. E. Ecke, “Fluid mixing in stratified gravity
489 currents: the prandtl mixing length,” *Physical review letters* **102**, 134504 (2009).
- 490 ⁴¹S. Balasubramanian and Q. Zhong, “Entrainment and mixing in lock-exchange gravity
491 currents using simultaneous velocity-density measurements,” *Physics of Fluids* **30**, 056601
492 (2018).

- 493 ⁴²T. Agrawal, B. Ramesh, S. Zimmerman, J. Philip, and J. C. Klewicki, “Probing the
494 high mixing efficiency events in a lock-exchange flow through simultaneous velocity and
495 temperature measurements,” *Phys. Fluids* **33**, 016605 (2021).
- 496 ⁴³P. Mukherjee and S. Balasubramanian, “Energetics and mixing efficiency of lock-exchange
497 gravity currents using simultaneous velocity and density fields,” *Physical Review Fluids* **5**,
498 063802 (2020).
- 499 ⁴⁴P. Mukherjee and S. Balasubramanian, “Diapycnal mixing efficiency in lock-exchange grav-
500 ity currents,” *Phys. Rev. Fluids* **6**, 013801 (2021).
- 501 ⁴⁵P. Monti, H. Fernando, and M. Princevac, “Waves and turbulence in katabatic winds,”
502 *Environ Fluid Mech* **14**, 431–450 (2014).
- 503 ⁴⁶C. Charrondière, C. Brun, J.-M. Cohard, J.-E. Sicart, M. Obligado, R. Biron, C. Coulaud,
504 and H. Guyard, “Katabatic winds over steep slopes: overview of a field experiment de-
505 signed to investigate slope-normal velocity and near-surface turbulence,” *Boundary-Layer*
506 *Meteorology* , 1–26 (2021).
- 507 ⁴⁷P. Odier, J. Chen, and R. Ecke, “Understanding and modeling turbulent fluxes and en-
508 trainment in a gravity current,” *Physica D: Nonlinear Phenomena* **241**, 260–268 (2012).
- 509 ⁴⁸Yang, Adam JK and Tedford, EW and Olsthoorn, J and Lawrence, GA, “Asymmetric
510 Holmboe instabilities in arrested salt-wedge flows,” *Physics of Fluids* **34**, 036601 (2022).
- 511 ⁴⁹M. E. Negretti, D. Zhu, and G. Jirka, “The effect of bottom roughness in two-layer flows
512 down a slope,” *Dyn. Oceans Atm.* **45**, 46–68 (2008).
- 513 ⁵⁰J. Eriksson, R. Karlsson, and J. Persson, “An experimental study of a two-dimensional
514 plane turbulent wall jet,” *Experiments in fluids* **25**, 50–60 (1998).
- 515 ⁵¹C. Buckee, B. Kneller, and J. Peakall, “Turbulence structure in steady, solute-driven
516 gravity currents,” *Particulate gravity currents* , 173–187 (2001).
- 517 ⁵²L. Ottolenghi, C. Adduce, R. Inghilesi, F. Roman, and V. Armenio, “Mixing in lock-release
518 gravity currents propagating up a slope,” *Phys. Fluids* **28**, 056604 (2016).
- 519 ⁵³B. Morton, G. I. Taylor, and J. S. Turner, “Turbulent gravitational convection from
520 maintained and instantaneous sources,” *Proceedings of the Royal Society of London. Series*
521 *A. Mathematical and Physical Sciences* **234**, 1–23 (1956).
- 522 ⁵⁴M. Princevac, H. Fernando, and C. D. Whiteman, “Turbulent entrainment into natural
523 gravity-driven flows,” *Journal of Fluid Mechanics* **533**, 259–268 (2005).

524 ⁵⁵M. Wells, C. Cenedese, and C. Caulfield, “The relationship between flux coefficient and
525 entrainment ratio in density currents,” *Journal of Physical Oceanography* **40**, 2713–2727
526 (2010).

527 ⁵⁶C. Cenedese and C. Adduce, “Mixing in a density-driven current flowing down a slope in
528 a rotating fluid.” *J. Fluid Mech.* **604**, 369–388 (2008).

529 ⁵⁷V. Alavian, “Behavior of density currents on an incline,” *Journal of hydraulic engineering*
530 **112**, 27–42 (1986).

531 ⁵⁸C. Cenedese and C. Adduce, “A new parameterization for entrainment in overflows.”
532 *J. Phys. Oceanogr.* **40**, 1835–1850 (2010).

533 ⁵⁹T. Gray, J. Alexander, and M. R. Leeder, “Longitudinal flow evolution and turbulence
534 structure of dynamically similar, sustained, saline density and turbidity currents,” *Journal*
535 *of Geophysical Research: Oceans* **111** (2006).

536 ⁶⁰B. Kneller, S. Bennett, and W. McCaffrey, “Velocity and turbulence structure of density
537 currents and internal solitary waves: potential sediment transport and the formation of
538 wave ripples in deep water,” *Sedimentary Geology* **112**, 235–250 (1997).

539 ⁶¹M. I. Cantero, S. Balachandar, M. H. García, and D. Bock, “Turbulent structures in
540 planar gravity currents and their influence on the flow dynamics,” *Journal of Geophysical*
541 *Research: Oceans* **113** (2008).

542 ⁶²S. B. Pope, *Turbulent flows* (Cambridge university press, 2000).

543 ⁶³L. Prandtl, “The generation of vortices in fluids of small viscosity,” *The Aeronautical*
544 *Journal* **31**, 718–741 (1927).

545 ⁶⁴W. D. Smyth and J. N. Moum, “Length scales of turbulence in stably stratified mixing
546 layers,” *Physics of Fluids* **12**, 1327–1342 (2000).

547 ⁶⁵C. Bluteau, N. Jones, and G. Ivey, “Turbulent mixing efficiency at an energetic ocean
548 site,” *Journal of Geophysical Research: Oceans* **118**, 4662–4672 (2013).

549 ⁶⁶R. Antonia and B. Pearson, “Effect of initial conditions on the mean energy dissipation
550 rate and the scaling exponent,” *Physical Review E* **62**, 8086 (2000).

551 ⁶⁷P. Doron, L. Bertuccioli, J. Katz, and T. Osborn, “Turbulence characteristics and dissi-
552 pation estimates in the coastal ocean bottom boundary layer from piv data,” *Journal of*
553 *Physical Oceanography* **31**, 2108–2134 (2001).

554 ⁶⁸D. Xu and J. Chen, “Accurate estimate of turbulent dissipation rate using piv data,”
555 *Experimental Thermal and Fluid Science* **44**, 662–672 (2013).

- 556 ⁶⁹J. V. Steinbuck, P. L. Roberts, C. D. Troy, A. R. Horner-Devine, F. Simonet, A. H.
557 Uhlman, J. S. Jaffe, S. G. Monismith, and P. J. Franks, “An autonomous open-ocean
558 stereoscopic piv profiler,” *Journal of Atmospheric and Oceanic Technology* **27**, 1362–1380
559 (2010).
- 560 ⁷⁰H. Tennekes, J. L. Lumley, J. L. Lumley, *et al.*, *A first course in turbulence* (MIT press,
561 1972).
- 562 ⁷¹M. M. Maqueda, A. Willmott, and N. Biggs, “Polynya dynamics: a review of observations
563 and modeling,” *Rev. Geophys.* **42(1)**, – (2004).
- 564 ⁷²C. Charrondière, C. Brun, J.-E. Sicart, J.-M. Cohard, R. Biron, and S. Blein, “Buoyancy
565 effects in the turbulence kinetic energy budget and reynolds stress budget for a katabatic
566 jet over a steep alpine slope,” *Boundary-Layer Meteorology* **177**, 97–122 (2020).
- 567 ⁷³R. T. McNider, “A note on velocity fluctuations in drainage flows,” (1982).